*Journal of Applied Polymer Science*

WILEY

Applied Polymer SCIENCE

RESEARCH ARTICLE OPEN ACCESS

# Systematic Study of PDMS Optical Waveguides for Pressure Sensing Using Design of Experiments

Camila A. Zimmermann | Bora Ung

Department of Electrical Engineering, École de Technologie Supérieure, Université du Québec, Montreal, Québec, Canada

**Correspondence:** Camila A. Zimmermann (camila-aparecida.zimmermann.1@ens.etsmtl.ca) | Bora Ung (bora.ung@etsmtl.ca)

**Received:** 28 October 2025 | **Revised:** 28 December 2025 | **Accepted:** 29 December 2025

**Keywords:** design of experiments | elastomers | mechanical properties | optical properties | poly(dimethylsiloxane) | polymer optical waveguides | pressure sensing | properties | sensors and actuators | structure–property relationships

## ABSTRACT

Poly(dimethylsiloxane) (PDMS) optical waveguides are highly regarded for pressure and tactile sensing due to their high sensitivity in the low-pressure range (0–100 kPa), desirable optomechanical properties, and biocompatibility. While it is known that PDMS properties are tunable via mix ratio and cure conditions, the magnitude of their effects and interactions remains unclear. To address this, response surface methodology was used to quantify the influence of mix ratio and cure conditions on key optical and mechanical properties of PDMS optical waveguides. Significant curvature was observed in the response surfaces for transverse compression sensitivity, secant modulus, and refractive index (RI). The mix ratio was the most significant factor for sensitivity and modulus, followed by a significant interaction with cure temperature. Cure temperature significantly influenced the RI, primarily due to density changes, while propagation loss showed a weak, yet statistically significant, linear dependence on mix ratio. These statistical findings are interpreted within the context of polymer science linking the empirical models to material behavior. By applying design of experiments, this work provides a systematic framework for understanding the relationship between fabrication parameters and the response of PDMS optical waveguides towards predictable and repeatable properties.

## 1 | Introduction

Over the last decade, poly(dimethylsiloxane) (PDMS) optical waveguides have emerged as a suitable candidate for the fabrication of optomechanical sensors responsive to bending, stretching, and compression [1]. For instance, PDMS optical waveguides have been proposed for biomedical pressure sensing [2–5], tactile and distributive sensing [6–11], and wearables and smart textiles [12–16], to cite a few. Typically, such optical waveguides operate through intensity modulation, offering a straightforward fabrication and operation. Their working principle relies on deformation of the optical path and local changes in refractive index (RI) (stress-optic effect) when subjected to an external force [17, 18]. These changes disrupt total internal reflection, which is crucial for waveguiding, causing some light to escape, thereby reducing the light intensity reaching the detector. Compared to mechanical sensors based on capacitive and resistive mechanisms [19, 20], optical waveguide intensity-modulated sensors offer immunity to electromagnetic interference and corrosion, a simplified design that does not require layers or the combination of dissimilar materials, and the ability to perform multiparameter multiplexing [19–21].

In addition to these key features, PDMS is advantageous over other optically transparent polymers commonly used in optical waveguiding such as polystyrene (PS), poly(methyl methacrylate) (PMMA), and poly(carbonate) (PC) thanks to a high stretchability and a modulus of elasticity three orders of magnitude lower [1, 17, 22]. The lower stiffness is associated with a higher sensitivity to low pressures [2, 5, 23], which combined with PDMS' biocompatibility [1, 24, 25], is particularly interesting in applications that require direct contact

with [2, 5, 13, 20, 26], or mimic soft tissues [8, 27]. In this context, reference pressure values up to 100 kPa are considered appropriate for tactile sensing [28, 29], while those reaching 600 kPa fall within the biomedical relevance range [21, 30–32]. Moreover, unlike thermoplastic elastomers [17, 33–35], PDMS is typically supplied as a two-component formulation consisting of a prepolymer base and a curing agent, whose processing can be achieved at room conditions and without the use of harsh solvents. Its mechanical and optical properties are also easily tailorable by varying the base-to-curing agent mix ratio and cure conditions [1, 36].

The ability to fine-tune PDMS optical and mechanical properties through variations in mix ratio and cure conditions has been a subject of several studies, as extensively discussed in our recent review article [1]. It includes efforts to establish empirical polynomial models between these processing parameters and RI, tensile and compressive moduli [37, 38]. Nonetheless, such models are limited to curing temperatures above 100°C and mix ratios with an excess of curing agent only. Besides, the influence of these variables on PDMS properties remains unclear and inconsistent, even for a widely studied commercial PDMS such as Sylgard 184 (Dow Chemical). For example, studies on the relationship between curing agent concentration and RI have yielded conflicting results, with some showing a peak RI at a specific mix ratio, decreasing with higher or lower curing agent concentrations [39, 40], while others reported a continuous increase in RI with increasing curing agent [37, 38, 41]. Similar discrepancies exist for tensile and compressive moduli [1, 42]. Numerous factors (e.g., PDMS batch variation, contamination, sample geometry, experimenter bias, processing and testing methods) complicate the establishment of a clear correlation between variables based on existing literature, as recently addressed in a meta-analysis on PDMS mechanical properties [42].

Considering the aforementioned, the aim of this work is to better understand the PDMS optical waveguides response surface regarding four key properties: sensitivity to transverse compression, secant modulus, RI, and propagation loss. For that, this study employed a design of experiments (DoE) to systematically plan, assess, and quantitatively estimate effects and interactions of varying Sylgard 184 mix ratios and cure conditions. DoE is a powerful and efficient statistical tool compared to other experimental strategies. It allows for the simultaneous variation of multiple parameters, using a reduced sample size while identifying key factors and possible interactions between experimental parameters [43, 44]. Empirical models relating the responses to the input parameters were obtained through this statistical methodology. The results were interpreted using supporting tests. This represents, to our knowledge, the first DoE-based analysis of PDMS optical and mechanical properties. This work provides a more quantitative and reproducible research framework for future studies and a clearer understanding of the influence of processing parameters on property trends. Furthermore, a linear correlation between secant modulus and sensitivity to transverse compression is reported. Although a correlation between both variables is expected and has been previously mentioned, this is the first time it has been demonstrated.

## 2 | Materials and Methods

A Face-Centered Central Composite Design (FC-CCD) was employed to investigate the influence of mix ratio and cure conditions on PDMS optical waveguides and free-standing films. This response surface methodology, compared to other central composite designs, uses only points within the originally defined factor ranges. Unlike a full factorial design, the FC-CCD enables the estimation of system curvature [43, 44], which is critical for capturing the anticipated non-linear behavior of PDMS's optical and mechanical properties under varying conditions [1].

Mix ratio and cure temperature were selected as primary factors due to their critical impact on the PDMS crosslinking network and related properties [1, 3, 37]. Sylgard 184 was selected as the representative material given its widespread use [23, 42, 45, 46]. Other parameters, such as sample geometry and mixing method, were held constant to maintain a manageable design space. The levels for each factor were chosen based on prior research exploring Sylgard 184 mix ratios from 1:1 to 30:1 and diverse cure conditions [3, 23, 39, 47–49]. The selected levels for the weight ratio of prepolymer base to curing agent and cure temperature are listed in Table 1, resulting in a total of 9 combinations.

Mix ratios equidistant from the recommended 10:1 ratio [50] were selected, i.e., 2:1 and 18:1, representing a sufficiently broad range for statistically significant responses. This range ensures comprehensive coverage of both curing-agent-rich and prepolymer-rich regimes. In terms of cure conditions, cure temperature was chosen as the primary factor. Recognizing the interdependence of cure time and cure temperature [45], the former was determined as a function of the latter to avoid incompatible combinations that would lead to a poorly cured PDMS. For this reason, "cure temperature" was used as input in the design (Table 1) and will be used hereafter to refer to the combined cure conditions. The minimum cure time at each temperature level was then selected based on the Sylgard 184 technical datasheet cure time recommendations and studies on PDMS curing kinetics. Specifically, Sylgard 184 technical datasheet recommends at least 48 h of cure at 25°C, and 10 min at 150°C [50]. Studies indicate that Sylgard 184 (10:1 and 1:1 ratios) cured at room temperature (22°C) reaches a plateau in oscillatory shear properties

**TABLE 1** | Proposed two-factor, three-level FC-CCD matrix: coded levels, actual experimental values, and design input values.

| Coded level | Mix ratio (Base:Curing agent) | FC-CCD mix ratio input | Curing conditions | FC-CCD cure temperature input |
|---|---|---|---|---|
| Low (−1) | 2:1 | 2 | 22°C (96 h) | 22 |
| Middle (0) | 10:1 | 10 | 86°C (65 min) | 86 |
| High (1) | 18:1 | 18 | 150°C (12 min) | 150 |

after 20–25 h, indicating solidification [3, 23]. Consequently, a 96-h duration was deemed sufficient to ensure PDMS crosslinking at 22°C. For the intermediate temperature of 86°C, a 1-h cure time was chosen, aligning with previous research using similar temperatures (80°C–85°C) and cure times ranging from 30 min to 1 h [2, 51–53]. Additionally, similar tensile modulus of elasticity has been reported for cure times of 60 and 90 min, demonstrating the formation of a stable network already in 1 h [52]. Preliminary testing confirmed that a 1-h cure at 86°C yielded waveguides with a non-tacky surface and good stretch resistance. Furthermore, Bardelli et al. reported a 90% conversion rate at 85°C after 13 min under isothermal conditions [45]. To compensate for oven ramp-up time, the cure times at 86°C and 150°C were increased by 5 and 2 min, respectively.

## 2.1 | Materials and Sample Fabrication

PDMS waveguides (Sylgard 184, Dow Corning) were fabricated using square ABS tubes, yielding cuboid samples averaged $1.20 \pm 0.07$ mm in side length. The side length was measured with a micrometer gauge with a flat circular presser footer (accuracy within 1% = 0.01 mm) by gently lowering it to the waveguide, as recommended by ASTM-D3767-03 (2020) [54]. This geometry simplifies transverse compression property determination, assuming constant contact area throughout testing [55]. To emulate conditions from a concurrent study, 300 µL of benzene was added to the base prepolymer. The mixture was stirred in an open beaker under a fume hood at ambient conditions until 98 wt% of the solvent had evaporated (approx. 4 h), as monitored by weight loss. Subsequently, the curing agent was added, and the mixture was manually stirred for 2 min, degassed under vacuum, and injected into ABS tubes using a syringe. To minimize the variability associated with manual mixing, beaker size (10 mL), sample volume (4 mL), and mixing time were standardized during sample preparation. After PDMS curing (Table 1) and a subsequent 4-day storage period at room conditions, the ABS tubes were dissolved in acetone to extract the waveguides. Acetone dissolved the ABS tubes within 10 min, whereas the waveguides remained intact due to the poor solubility of PDMS in acetone [56]. In parallel with the waveguide fabrication, free-standing films were prepared using a mold and casting technique. Aluminum weighing pans with a diameter of 4.3 cm were used as molds, and approximately 1 mL of the PDMS mixture was dispensed into each pan. After curing, the films were carefully peeled from the molds and then cut into four rectangular stripes, each measuring $8 \times 20$ mm$^2$. The average thickness of these films was determined to be $606 \pm 52$ µm. All samples were fabricated in an interval of 4 days and stored in the dark in ambient conditions (22.0°C ± 0.3°C, 56% ± 3% RH) for 7 weeks before undergoing further testing. SMA connectors were attached to the waveguide ends using silicone ferrules cut from commercial silicone tubing.

## 2.2 | Statistical Analysis

Both two-way ANOVA with post hoc comparisons (for the data presented in Tables 2 and 4) and response surface methodology (FC-CCD) were performed using Minitab software (version 22.3) with a confidence level of 95% ($\alpha = 0.05$). Prior to the two-way ANOVA for each measured property, normality (Ryan-Joiner test for each combination) and homogeneity of variances (Levene's test) were assessed. These assumptions were confirmed for all properties, with the exception of propagation loss, where the limited number of replicates prevented a formal test of homogeneity of variances. The two-way ANOVA was employed to test the significant effects of the two factors (mix ratio and cure temperature) on each measured property. In cases where significant effects were found, the Tukey method was subsequently used for post hoc pairwise comparison of means, identifying which specific combinations of factors were significantly different from each other. The number of replicates varied based on the measured property, with all FC-CCD points replicated at least twice. This approach, departing from the usual practice of replicating only the center point for error estimation, increased the number of experimental runs. However, it provided a more thorough understanding and estimation of the error across the design space, which was particularly valuable given the inherent variability in mechanical testing [36]. Runs were randomized during data collection. Compression sensitivity and secant modulus response surface analysis included blocks to account for data collection on different dates. All terms were included in the full-quadratic regression models.

## 2.3 | Optomechanical Testing

Transverse compression testing was performed using an Alliance RF/200 testing machine (MTS Systems Corporation, USA). The testing setup included an aluminum base and an aluminum indenter with a contact area of $0.8 \times 15$ mm$^2$ connected to one of three load cells (10, 100, or 1000 N) to accommodate varying force ranges (Figure S1). The 10 N load cell (average noise of $0.0028 \pm 0.0008$ N) was specifically chosen for measurements at low deformations and low stress levels to achieve optimal signal resolution. The 100 and 1000 N load cells (average noise of $0.023 \pm 0.006$ and $0.21 \pm 0.05$ N, respectively) were employed to extend the testing range to higher compression values up to failure. The aluminum base was leveled in $x$ and $y$ axes using a 3D stage mounted on a breadboard to ensure a uniform force distribution on the waveguide contact area. The indenter was carefully centered and aligned directly above the waveguide without initial contact or preload. The true zero point was determined as the onset of force increase. Quasi-static compression was applied at a crosshead displacement rate of 0.001 mm/s (0.06 mm/min, ~0.0008/s strain rate). All tests were carried out at 22.5°C ± 0.7°C and 26% ± 7% RH.

Nominal stress ($\sigma$) was calculated as $F / A_i$, where $A_i$ represents the contact area between the indenter and the waveguide. Nominal strain ($\varepsilon$) was calculated as $\Delta L / L_i$, with $L_i$ denoting the initial side length of the waveguide. For optical characterization, waveguides were coupled to a non-polarized white light source (peak at 660 nm, HL-2000-HP, Ocean Optics Inc.) via a 600-µm optical fiber (QP600-025-SR-BX, Ocean Optics Inc.). The light transmitted through the waveguide was then analyzed using a high-resolution spectrometer (HR4000CG, Ocean Optics Inc.). The spectrometer's integration time was adjusted to achieve approximately 14,000 counts (approx. 2000 µs), with a data acquisition rate of 1 Hz. The optical peak intensity at 664 nm was normalized to its initial value ($I \times 100 / I_0$). Time synchronization of mechanical and optical data and optomechanical data processing was performed using Matlab software R2024a.

### 2.4 | Refractive Index Measurement

The RI of the free-standing films was determined using an Abbe refractometer (AR-2, Azzota LLC) illuminated with ambient light (peak wavelength of 603 nm). The temperature ($T$) at the end of each measurement was used to calculate the RI at a standardized temperature of 20°C ($RI^{20} = RI^{T} + 0.00045(T - 20)$).

### 2.5 | Propagation Loss

The cutback method was used to determine the propagation loss of the waveguides coupled to the HL-2000-HP white light source with peak wavelength of 660 nm. The transmitted optical power was measured using a photodiode (S120C, Thorlabs Inc.) connected to a power meter interface (PM100USB, Thorlabs Inc.). The waveguides were cut into 1 cm increments using a razor blade. The total optical loss in dB, calculated as $10\log_{10}\left(P_{in}/P_{out}\right)$, was plotted as a function of the waveguide's propagation length (cm) and the slope of the resulting linear fit was taken as the propagation loss.

### 2.6 | Density

Density of selected samples was determined using a helium pycnometer (Ultrapyc 5000, Antoon Paar) in pulse mode. Results are reported as an average of 5 to 10 runs.

### 2.7 | Crosslink Density and Sol Fraction Determination

The crosslink density ($\upsilon$) was determined via equilibrium swelling tests conducted at room temperature (22°C), adapted from methods found in the literature [3, 57, 58]. First, the PDMS waveguides were cut into smaller pieces, transferred to glass vials (approximately 90 mg per vial), and their initial mass ($m_i$) was recorded. Then, 4.5 mL of chloroform (Sigma-Aldrich, ≥99.5%) was added to each vial. After 24 h of immersion, the chloroform extracts were replaced with fresh chloroform. Following another 28 h of immersion in chloroform, the samples were removed from the solvent and allowed to dry under a fume hood for 66 h at room temperature. Subsequently, the samples were swollen in toluene (Sigma-Aldrich, ≥99.5%) for 96 h. Excess toluene was carefully removed with lint-free wipes, and the swollen samples were immediately weighed ($m_{sw}$). Finally, the samples were left to dry for another 66 h, and the final dry mass recorded ($m_{dry}$). The sol fraction, dry polymer density after extraction ($\rho$), volume fraction of polymer in the swollen network ($\phi_p$), and crosslink density assuming a phantom network were calculated using Equations (1–5) [58, 59].

$$sol\ fraction\ (\%) = \frac{m_i - m_{dry}}{m_i} \times 100 \tag{1}$$

$$\rho = \rho_0\left(1 - \frac{sol\ fraction}{100}\right) \tag{2}$$

$$\phi_p = \frac{1}{\frac{\rho}{\rho_s}\left(\frac{m_{sw}}{m_{dry}} - 1\right) + 1} \tag{3}$$

$$\upsilon = -\frac{\ln\left(1-\phi_p\right) + \phi_p + \chi{\phi_p}^2}{V_s\left(V_0{\phi_p}^{2/3} - \frac{2\phi_p}{f}\right)} \tag{4}$$

$$\chi = 0.44 + 0.36\phi_p \tag{5}$$

where $\rho_0$ is the average polymer density measured by helium pycnometry (1.046 ± 0.004 g/cm$^3$), $\rho_s$ is the solvent density (toluene, 0.865 g/cm$^3$) [58], $V_s$ is the molar volume of the solvent (106.52 cm$^3$/mol) [58], $V_0$ is the volume fraction of linked chains in the dry polymer network which is equal to 1, as the free chains were previously extracted (Figure S2), $\chi$ is the toluene-PDMS interaction parameter (Equation 5), and $f$ is the functionality of the crosslinks, assumed to be 4 [58, 59].

## 3 | Results and Discussion

Rounded-square cross-section PDMS optical waveguides (Figure 1a) were fabricated following the conditions outlined in Table 1, by mixing the base polymer with the curing agent and injecting the resulting liquid mixtures into square ABS tubes. Following the curing process, the optical waveguides with average side length of 1.20 ± 0.07 mm and 13.5 cm long were retrieved by dissolving the mold. To assess their response to transverse compression, the waveguides were coupled to a white light source and a spectrometer and subjected to compression between an aluminum base and an indenter using a testing machine (Figure 1b and Figure S1). Figure 1c illustrates the principle of light guiding via total internal reflection (TIR) in the initial unloaded state. In air-clad optical waveguides, such as those used in this work, the RI of the core ($n_1$) is higher than that of the surrounding medium ($n_2$, air), which is a fundamental requirement for TIR. TIR is sustained provided the angle of incidence $\theta$ exceeds the critical angle, defined as $\theta_c = \sin^{-1}\left(n_2/n_1\right)$ [60]. Upon the application of transverse compression (Figure 1d), the waveguide undergoes mechanical deformation. This introduces geometric perturbations (such as macrobending) and local RI changes [17, 18]. When the local incidence angle drops below the critical angle ($\theta < \theta_c$), the TIR condition is violated. Consequently, a portion of the light refracts out of the core ($I_r$) causing optical loss [17, 60]. This light outcoupling results in a reduced optical output intensity ($I_0 - I_r$), which correlates to the applied pressure.

The PDMS optical waveguides presented a non-linear change in normalized transmitted optical intensity as a function of compressive stress, as shown in Figure 2a. Thus, sensitivity to compression ($S_{100kPa}$) was determined as the slope of the best linear fit ($0.94 < R^2 < 0.99$) up to a compressive stress of 100 kPa, as given in Figure 2b. A compressive stress of 100 kPa, corresponding to strains between 8% and 17%, falls within the approximate range where Hooke's law ($\sigma = E\varepsilon$) remains reasonably valid for silicone elastomers (i.e., 10%–15% strain) [36, 57, 61], and is relevant to both tactile [28, 29] and biomedical [21, 30–32] applications. Depending on the optomechanical behavior of the waveguides, it was possible to extend the pseudo linear range with a good fit to higher stresses values as given in Table S1.

To better understand the relationship between sensitivity and compressive elastic modulus, the latter was calculated using the

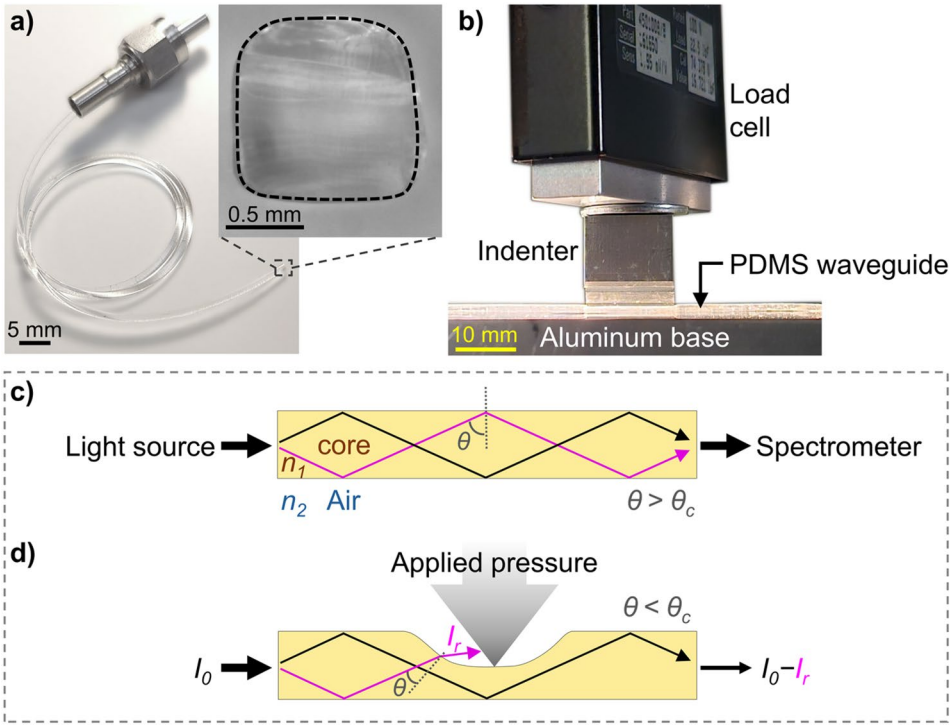


**FIGURE 1** | (a) Representative picture of a PDMS optical waveguide, with an inset depicting the respective cross-sectional micrograph. (b) Close-up picture of the PDMS optical waveguide positioned between the indenter and the aluminum base during the compression experiment. (c) Schematic diagram illustrating the waveguide working mechanism. [Color figure can be viewed at wileyonlinelibrary.com]

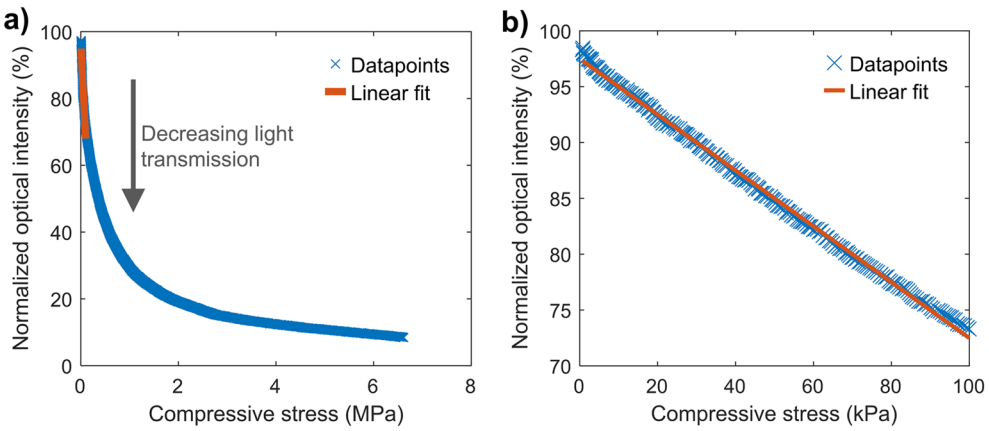


**FIGURE 2** | Normalized transmitted optical intensity as a function of applied stress. (a) Full experimental range, including a linear fit (orange line) for the region up to 100 kPa. (b) Detailed view of the low-stress regime (0–100 kPa) highlighting the linear response. [Color figure can be viewed at wileyonlinelibrary.com]

secant modulus approach for a compressive stress of 100 kPa. While ASTM D638-14 is primarily a tensile testing standard, its principles for secant modulus calculation were adapted for transverse compression [62], because of the typical non-linear stress–strain behavior characteristic of PDMS elastomers under tension or compression. In addition to sensitivity to compression and secant modulus ($E_{100kPa}$), RI under ambient light and white light propagation loss were also measured considering their relevance in optical waveguiding. The corresponding means for the measured properties of the nine combinations are given in Table 2.

The compression sensitivity up to 100 kPa of the PDMS waveguides prepared at a 2:1 mix ratio and cured at 150°C (02-150) in this study (Table 2) is slightly lower but aligns reasonably well to that reported for microfluidic wet-spun PDMS waveguides fabricated at a 1:1 mix ratio (−0.40%/kPa) [23], despite inherent methodological variations. In contrast, the sensitivity of the 10–150 optical waveguides was nearly double that reported for waveguides fabricated at a 10:1 mix ratio and cured at 125°C for 37 min (−0.06%/kPa) [3]. Furthermore, the secant moduli ($E_{100kPa}$, Table 2) trend showed good agreement with literature [13, 61, 63–65], with deviations from the 10:1 mix ratio generally resulting in lower moduli. The effect of cure temperature on the secant modulus was mix ratio-dependent. At a 2:1 ratio, the modulus decreased with increasing temperature, whereas at 10:1, no significant temperature dependence was found. An inverse trend was observed for the 18:1 ratio.

**TABLE 2** | FC-CCD combinations and their corresponding responses.

| Mix ratio (Base: Curing agent) | Cure T (°C) | Label | $S_{100kPa}$(−%/kPa) ($n=5$) | $E_{100kPa}$ (MPa) ($n=5$) | RI at 20°C ($n=4$) | Propagation loss (dB/cm) ($n=2$) |
|---|---|---|---|---|---|---|
| 2:1 | 22 | 02-022 | $0.21\pm0.03^{a}$ | $0.86\pm0.01^{a}$ | $1.4126\pm0.0001^{a}$ | $0.26\pm0.02^{a}$ |
| | 86 | 02-086 | $0.22\pm0.03^{a}$ | $0.77\pm0.02^{b}$ | $1.4136\pm0.0001^{b}$ | $0.25\pm0.02^{a}$ |
| | 150 | 02-150 | $0.35\pm0.01^{b}$ | $0.60\pm0.01^{c}$ | $1.4137\pm0.0002^{bc}$ | $0.24\pm0.02^{a}$ |
| 10:1 | 22 | 10-022 | $0.14\pm0.01^{c}$ | $1.19\pm0.02^{d}$ | $1.4131\pm0.0001^{d}$ | $0.25\pm0.01^{a}$ |
| | 86 | 10-086 | $0.10\pm0.01^{c}$ | $1.22\pm0.03^{d}$ | $1.4139\pm0.0002^{c}$ | $0.23\pm0.01^{a}$ |
| | 150 | 10-150 | $0.12\pm0.02^{c}$ | $1.21\pm0.01^{d}$ | $1.4139\pm0.0001^{c}$ | $0.25\pm0.01^{a}$ |
| 18:1 | 22 | 18-022 | $0.26\pm0.01^{a}$ | $0.63\pm0.03^{ce}$ | $1.4129\pm0.0001^{d}$ | $0.27\pm0.01^{a}$ |
| | 86 | 18-086 | $0.21\pm0.04^{a}$ | $0.64\pm0.03^{e}$ | $1.4136\pm0.0001^{b}$ | $0.27\pm0.04^{a}$ |
| | 150 | 18-150 | $0.22\pm0.03^{a}$ | $0.70\pm0.02^{f}$ | $1.4137\pm0.0001^{b}$ | $0.28\pm0.02^{a}$ |

*Note:* Means within a column sharing the same superscript letter are not significantly different ($p\leq0.05$), and $n$ denotes the number of replicates per combination.

The lower secant modulus of the 02-150 PDMS waveguides compared to those cured at lower temperatures (02-022 and 02-086), along with the lack of cure temperature dependence for the 10:1 mix ratio, were unexpected, as higher cure temperatures typically yield stiffer PDMS [1]. To address these discrepancies, we first considered the potential aging effect, as it has been shown that the modulus of freshly prepared PDMS samples strongly depends on curing time and temperature, changing significantly over 4 weeks [66]. Furthermore, aged PDMS exhibited mechanical properties similar to those of freshly prepared samples cured at higher temperatures or for longer periods [67]. In our study, samples were stored at room temperature for an additional 7 weeks between preparation and testing to promote crosslinking and stabilization of properties, a strategy supported by the long-term measurements provided in the Supporting Information (Table S2). We also investigated the possibility of a sample swap for 02-022 and 02-150 waveguides. Therefore, new 02-022 and 02-150 waveguides were prepared and tested within 10 days to: (i) verify any aging effect, and (ii) confirm the sample identity. These new samples replicated the original findings, with a lower secant modulus for the 02-150 waveguides and mean values not statistically different from those tested after 7 weeks. Supporting these results, a similar trend was reported for Sylgard 184 PDMS with a 6:1 mix ratio (excess of curing agent) [52]. For instance, under curing conditions similar to those used in this study (85°C for 60 min and 150°C for 15 min), reported tensile elastic moduli were 1.65 MPa and 1.57 MPa, respectively. In contrast, curing at room temperature resulted in a lower modulus of 1.30 MPa, which we attribute to insufficient aging time for complete property stabilization [52]. Additional experiments were conducted to further elucidate this behavior, and the results are presented later in Section 3.2.

As shown in Table 2, the lowest RI occurred for samples cured at 22°C across all mix ratios. RI values for samples cured at 86°C and 150°C were not significantly different, which is consistent with previously reported temperature dependencies [40, 53, 68]. The mean RI values were slightly higher for the 10:1 mix ratio across all cure temperatures, also aligning with previous observations [39, 40]. In terms of propagation loss, values across all tested combinations were comparable to those measured at 520–660 nm [3, 23, 69]. The variability in propagation loss was lower at the 10:1 mix ratio, likely due to the higher stiffness of these waveguides, which facilitated handling and alignment and reduced the potential for microbending contributions to optical loss. While not statistically significant (Table 2), the 18:1 mix ratio exhibited slightly higher propagation losses, potentially due to increased optical absorption from unreacted vinyl groups and Rayleigh scattering induced by inhomogeneities associated with unreacted chains [60] (see Section 3.2 for detailed discussion).

## 3.1 | FC-CCD Analysis

Response surface regression analysis using the FC-CCD was performed to identify and estimate the influence of the tested factors (mix ratio and cure temperature) and their interaction on $S_{100kPa}$, $E_{100kPa}$, RI, and propagation loss. The initial analysis included all linear and quadratic terms for mix ratio and cure temperature, as well as the interaction term. For $S_{100kPa}$ and $E_{100kPa}$, the equations were averaged over blocks to improve the precision of effect estimates, as data collection spanned several days. The resulting regression equations are presented in Equations (6–9).

$$S_{100kPa}\,(-\%/kPa)=0.2873-3.6\times10^{-2}A-4.9\times10^{-4}B+2.07\times10^{-3}A^{2}+9.36\times10^{-6}B^{2}-8.85\times10^{-5}AB \tag{6}$$

$$E_{100kPa}\,(MPa)=0.6321+0.1374A-1.49\times10^{-3}B-7.82\times10^{-3}A^{2}-3.11\times10^{-6}B^{2}+1.58\times10^{-4}AB \tag{7}$$

$$RI\,(a.u.)=1.4119+1.14\times10^{-4}A+2.59\times10^{-5}B-4.45\times10^{-6}A^{2}-9.7\times10^{-8}B^{2}-2.03\times10^{-7}AB \tag{8}$$

$$Prop.\ loss\,(dB/cm)=0.2717-4.47\times10^{-3}A-4.26\times10^{-4}B+2.61\times10^{-4}A^{2}+2.04\times10^{-6}B^{2}+8.10\times10^{-6}AB \tag{9}$$

where $A$ corresponds to the mix ratio (2, 10 or 18), and $B$ to the cure temperature (22°C, 86°C, or 150°C).

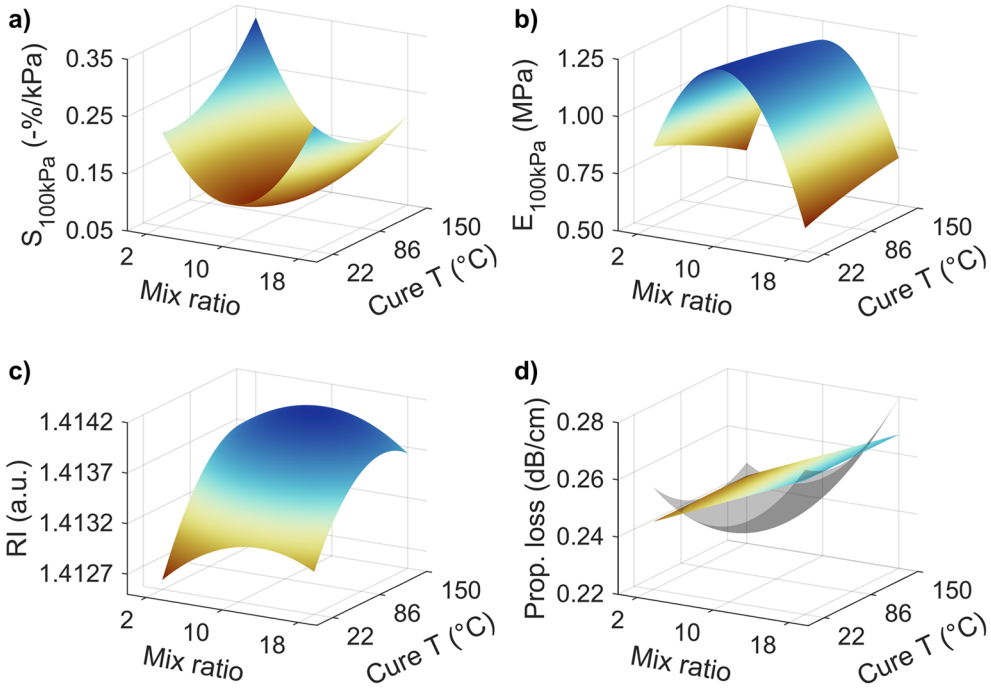


**FIGURE 3** | Response surface plots for (a) compression sensitivity up to 100 kPa, (b) secant modulus at 100 kPa, (c) refractive index, and (d) propagation loss. For plot (d), the gray and colored surfaces represent the models from Equation (9) (quadratic) and Equation (10) (linear), respectively. [Color figure can be viewed at wileyonlinelibrary.com]

The coefficient of determination ($R^2$) values indicate that the models explain 0.896, 0.985, 0.966, and 0.446 of the variability in $S_{100kPa}$, $E_{100kPa}$, RI, and propagation loss, respectively. The analysis of variance (ANOVA) results confirm that the models in Equations (6–8) are statistically significant ($p$-values $\leq 0.05$, Tables S3–S5), although Equations (6) and (7) also exhibited a significant lack-of-fit. This lack-of-fit can be attributed to the influence of other variables, including shear stress, sample alignment, waveguide surface roughness, and light scattering at interfaces, which were not accounted for in the models. For $E_{100kPa}$, the cure temperature quadratic term ($B^2$) $p$-value (Table S4) was greater than the significance level $\alpha = 0.05$, meaning that it is not statistically significant. Upon removing this term, the significance of the other model terms remained robust and the $R^2$ value was essentially unchanged, justifying the use of a reduced model. Regarding propagation loss, the initial response surface model (Equation 9) was not significant ($p$-value = 0.162, Table S6) likely due to the high variability in the measurements, reflected by the large standard deviations (Table 2) and an over-parameterized quadratic model. This considerable level of noise may have masked any underlying causal links even though standard deviations corresponding to 4%–15% of the mean are in line with previously published results [3]. Based on this, the model for the propagation loss (Equation 9) was simplified to consider only the significant mix ratio term ($A$), which yielded a statistically significant linear model, Equation (10), with a $p$-value of 0.045, a non-significant lack-of-fit ($p$-value = 0.458, Table S7), and an $R^2$ of 0.228.

$$Prop.\ loss\ (dB/cm) = 0.2408 + 1.446 \times 10^{-3} A \qquad (10)$$

Although this model's $R^2$ is lower than the initial 0.446, it is a more realistic measure of a weak but significant linear relationship between propagation loss and mix ratio, as indicated by the ANOVA results. The positive coefficient for the mix ratio can be attributed to an excess of light-absorbing vinyl groups at the 18:1 ratio, as the prepolymer base is present in excess. This observation highlights how the sign of the coefficients in the regression equations provides insight into the relationship between the factors and the measured properties. The corresponding response surface plots for the models in Equations (6) to (10) are shown in Figure 3.

Positive coefficients for the linear terms ($A$ and $B$) indicate that increasing the factor leads to an increase in the response. Conversely, negative coefficients indicate an inverse relationship. For the quadratic terms ($A^2$ and $B^2$), a positive coefficient corresponds to a concave-up curvature in the response surface plots, suggesting a minimum value within the investigated experimental range as shown in Figure 3a. A negative coefficient for the quadratic term indicates a concave-down curvature and a peak response (Figure 3b,c). When a negative linear term is combined with a positive quadratic term, the response decreases initially to a minimum before increasing again as the factor's value increases. For the interaction term ($AB$), a negative coefficient implies that the positive impact of one factor is reduced, or the negative impact is enhanced by the other factor. Moreover, response surface plots allow for the rapid identification of responsive regions. Notably, Figure 3a displays a sensitivity peak between 2:1 and 10:1 at higher cure temperatures, highlighting the region where system performance is most dependent on the tested parameters.

Considering the good quality of the residual plots (Figures S3–S5, and S7), one can state that the models are useful approximations, capturing most of the important relationships between variables and responses, even though they are not a perfect representation of the response surface. It is important to note that the regression models are valid strictly within the tested ranges and are specific

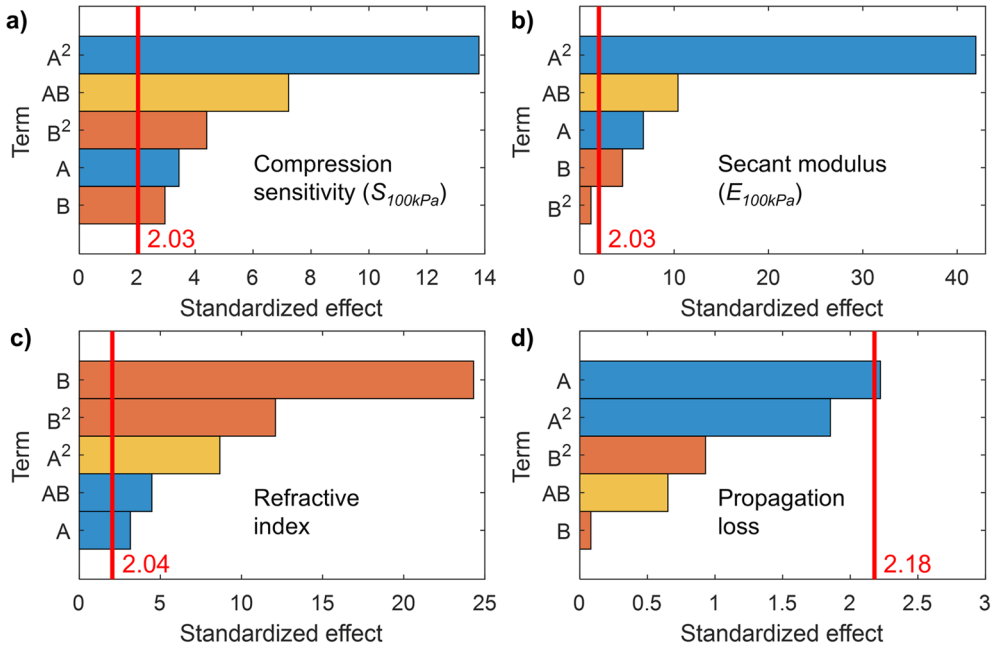


**FIGURE 4** | Pareto charts for (a) compression sensitivity, (b) secant modulus, (c) refractive index, and (d) propagation loss. The red line represents a reference threshold for statistical significance. [Color figure can be viewed at wileyonlinelibrary.com]

to the design space of Sylgard 184. Distinct PDMS formulations (e.g., Sylgard 186) or composites modified with nanofillers possess fundamentally different physicochemical characteristics such as variations in molecular weight, polydispersity index, and filler content that would inherently alter the response surface. Nevertheless, the DoE-based framework established in this work provides a robust and reproducible protocol that can be readily adapted to characterize and optimize these alternative polymer systems.

The magnitude and importance of all terms in the models (Equations 6–9) have been ranked using the Pareto chart of standardized effects as shown in Figure 4. The standardized effects are based on *t*-tests, with bars crossing the reference line representing terms that are statistically significant at the 0.05 significance level.

The Pareto charts (Figure 4a,b) show that the mix ratio quadratic term ($A^2$) is the most statistically significant factor influencing both $S_{100kPa}$ and $E_{100kPa}$ followed by a significant interaction with cure temperature (*AB* term). This aligns with the strong curvature along the mix ratio axis in the response surface plots (Figure 3a,b). For RI, cure temperature emerges as the primary factor (Figure 4c), in line with the statistically significant RI difference between samples cured at higher temperatures and those at 22°C (Table 2), and the pronounced curvature along the cure temperature axis in Figure 3c. This observation is consistent with the findings of Santiago-Alvaro et al. [38]. The Pareto chart related to the initial quadratic model of propagation loss (Figure 4d) visually confirms the ANOVA results (Table S6). It shows that the linear term for mix ratio is the only effect to cross the significance threshold ($\alpha = 0.05$), as previously discussed, supporting the decision to simplify the model to the linear regression shown in Equation (10).

The effect of cure temperature on RI is directly linked to density variations [39, 70], a behavior consistent with the Lorentz-Lorenz theory. For instance, samples with the lowest mean RI (02-022 and 18-022) exhibited densities of $1.0442 \pm 0.0027$ and $1.0449 \pm 0.0023\,g/cm^3$, respectively, whereas the sample with the highest mean RI (10–150) had a density of $1.0481 \pm 0.0026\,g/cm^3$. This relationship is further evidenced by the linear correlation between density and the Lorentz–Lorenz parameter, $(n^2 - 1)/(n^2 + 2)$, as shown in Figure 5. The calculated slope of $0.2385\,cm^3/g$ represents the specific refraction and aligns well with reported values for PDMS [70]. Higher cure temperatures promote volume shrinkage via polymer chain rearrangement and formation of a denser network, likely accompanied by the elimination of volatile compounds such as oligomers and solvents [71].

## 3.2 | Correlations Between Responses and Polymer Network Properties

Considering that the response surface plot of $S_{100kPa}$ closely resembles the inverted trend of the $E_{100kPa}$ one (Figure 3a,b), the former was plotted as a function of the latter in order to better understand the correlation between these two responses. The plot along with the linear regression equation is given in Figure 6.

Figure 6 shows the expected inverse relationship between waveguide secant modulus and sensitivity to transverse compression. Stiffer waveguides are less prone to deformation under compression, leading to lower optical attenuation and consequently reduced sensitivity [2, 23, 72]. The linear regression model reasonably describes the negative correlation between $S_{100kPa}$ and $E_{100kPa}$ with an $R^2$ of 0.813 and a root mean squared error (RSME) of 0.034. This RMSE represents approximately 12.4% of the total sensitivity range, which is notably high. While this linear model may not be suitable for precise

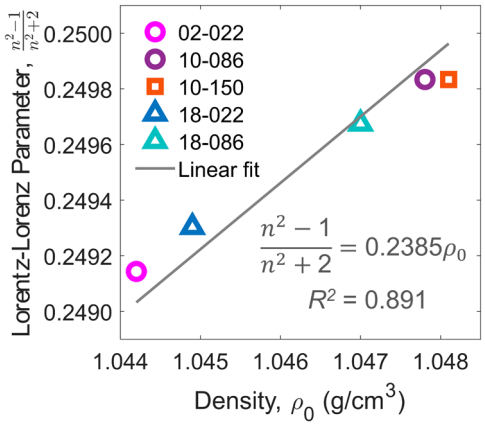


**FIGURE 5** | Lorentz–Lorenz optical parameter as a function of density for selected PDMS samples and the corresponding linear regression fit. [Color figure can be viewed at wileyonlinelibrary.com]

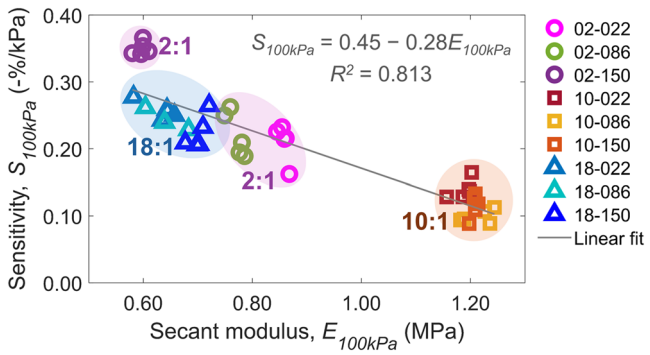


**FIGURE 6** | Correlation between $S_{100kPa}$ as a function of $E_{100kPa}$, and the corresponding linear regression fit. [Color figure can be viewed at wileyonlinelibrary.com]

predictions, it effectively captures a strong relationship for general trend analysis. Considering that PDMS modulus is dependent on the crosslink density and the amount of defects present in the network (e.g., loops, unreacted functional groups, branched and dangling chains) [36, 57, 73], we also determined the sol fraction and crosslink density via equilibrium swelling tests to further elucidate and support these findings. The results are presented in Table 3.

The 10-086 waveguides exhibited the highest crosslink density, which did not result in a statistically significant increase in their measured modulus compared to 10-022 and 10-150 (Table 2). Considering the general trends observed in this study, PDMS optical waveguides exhibiting the highest crosslink density and lowest sol fraction were consistently obtained at the manufacturer-recommended 10:1 mix ratio (Table 3), corroborating findings in the existing literature [3, 58, 65]. These results are expected as deviations from the 10:1 ratio, assumed to approximate the stoichiometric ratio between the prepolymer base and curing agent [39], lead to more defective networks, particularly with a higher concentration of unreacted functional groups. These defects decrease the fraction of elastically effective polymer network per unit volume responsible for the final PDMS mechanical properties [65, 73]. While acknowledging the limitations of equilibrium swelling experiments and the complexity of precisely quantifying PDMS network features, such as the nature and amount of defects,

**TABLE 3** | Extracted sol fraction (%) and crosslink density for all FC-CCD combinations.

| Sample | Sol fraction (%) | Crosslink density (×10$^{-4}$ mol/cm$^3$) |
|---|---|---|
| 02-022 | 9.50 ± 0.53 | 5.4 ± 0.28 |
| 02-086 | 12.32 ± 0.03 | 4.4 ± 0.02 |
| 02-150 | 12.30 ± 0.83 | 2.8 ± 0.05 |
| 10-022 | 5.01 ± 0.41 | 6.2 ± 0.18 |
| 10-086 | 5.01 ± 0.04 | 7.2 ± 0.07 |
| 10-150 | 5.02 ± 0.21 | 6.2 ± 0.20 |
| 18-022 | 9.37 ± 0.43 | 2.0 ± 0.14 |
| 18-086 | 9.23 ± 0.02 | 2.3 ± 0.12 |
| 18-150 | 8.51 ± 0.07 | 2.7 ± 0.01 |

and their influence on PDMS elastic properties, along with other parameters like precursor polydispersity index and filler content [73], our results support this conclusion.

For PDMS waveguides prepared with an excess of the prepolymer base (18:1 mix ratio), increasing cure temperature correlated with enhanced crosslink density and a concomitant reduction in sol fraction. This observation is consistent with the expectation that elevated temperatures likely promote the formation of more crosslinks by minimizing network defects and suppressing secondary reactions albeit the limitations imposed by an nonstoichiometric reaction [3, 58]. Conversely, an inverse trend was observed when the preparation conditions included an excess of curing agent, specifically in waveguides prepared at a 2:1 mix ratio (Table 3). It is generally accepted that increasing the amount of curing agent would lead to a decrease in the size of dangling chain defects within the polymer network leading to an increase in modulus and crosslink density [73]. However, this effect is likely limited to a certain extent, particularly when the concentration of Si—H groups significantly surpasses the total number of vinyl groups available for the crosslinking reaction. Analysis of the as-prepared waveguides via ATR-FTIR spectroscopy revealed that the relative amount of unreacted hydride groups (Si—H), calculated by the ratio $I_{2162}/I_{1012}$ (Figure S8, Table S8), was 3–5 times higher at the 2:1 mix ratio. This elevated level is attributed to the stoichiometric excess of the curing agent, which contains the Si—H functional group [3, 57]. We hypothesize that under these specific conditions, elevated cure temperatures accelerate the reaction rate, promoting the localized formation of network defects, particularly short chains. These species are excluded from the crosslinked network and may also act as plasticizers [57, 59]. In contrast, at room temperature (22°C), the slower reaction kinetics allow for greater diffusion of unreacted molecules within the mixture. This increased diffusion time enhances the probability of these molecules reacting with available functional groups, thereby increasing the crosslink density and reducing the population of elastically inactive defects. This hypothesis is corroborated by several observations: (i) the higher sol fraction measured for the 02-086 and 02-150 waveguides (Table 3), (ii) the lower relative amount of Si—H in the as-prepared 02–022 waveguides (Table S8), and (iii) a consistent reduction in the relative Si—H content for all waveguides prepared at the 2:1 mix ratio

following sol fraction extraction (Table S8). Furthermore, the 02-150 waveguides exhibited a crosslink density comparable to the 18-150 waveguides. However, the 02-150 material is softer, suggesting a more defective network structure that compromises its mechanical response.

Regarding the RI, the measured crosslink density (Table 3) did not exhibit a strong correlation with the observed RI values (Table 2). Instead, the RI trend is better explained by changes in bulk density, as previously discussed (Figure 5). We attribute this divergence to the distinct roles of the sol fraction and silica fillers in Sylgard 184. While crosslink density estimations effectively capture relative differences in the elastically active network and directly correlate with the modulus, they do not account for the sol component present in the bulk material. Furthermore, silica fillers interact with the polymer chains and introduce non-affine behavior during swelling, which does not translate equivalently to RI and density measurements.

Similarly, propagation loss was not directly proportional to crosslink density. Instead, optical attenuation in PDMS is primarily governed by the intrinsic absorption of chemical bonds and Rayleigh scattering arising from density fluctuations and material inhomogeneities [60]. Notably, the 18:1 mix ratio, which exhibited slightly higher propagation loss (Table 2), contains a large stoichiometric excess of the vinyl-containing prepolymer base. Due to the insufficient quantity of curing agent, a significant concentration of unreacted vinyl groups remains within the bulk material. Although UV–Vis spectra of the free-standing films revealed no specific absorption bands across all combinations (Figure S9a), the chloroform extracts (containing the sol fraction) for the 18:1 samples exhibited increased absorption in the 240–350 nm range attributed to $\pi \rightarrow \pi^*$ electronic transitions of vinyl groups (Figure S9b) [74]. While this absorption peaks in the UV range, at the extended optical path lengths characteristic of waveguides, it can manifest as an absorption tail extending into the visible range [74]. This likely contributes to the measured propagation loss, particularly given the use of a broadband white light source. Furthermore, the lower degree of crosslinking at 2:1 and 18:1 ratios results in a higher sol fraction (Table 3). The resulting abundance of free polymer chains could act as optical inhomogeneities, potentially increasing Rayleigh scattering compared to a tightly crosslinked network. However, the lack of statistical difference (Table 2) prevents definitive conclusions regarding this mechanism.

### 3.3 | Ultimate Properties and Cyclic Compression

The ultimate mechanical properties of all FC-CCD combinations under transverse compression, along with the behavior of selected waveguides under cyclic compression, were also evaluated to provide a comprehensive understanding of their performance. Figure 7 presents the corresponding stress–strain curves and Table 4 the average compressive strength and strain at break.

The compressive strength at break of the waveguides closely followed the trends previously observed for the secant modulus, exhibiting peak values at the 10:1 mix ratio and a significant temperature dependence for waveguides prepared at the 2:1 ratio (Table 4). Waveguides fabricated at the 10:1 ratio demonstrated the highest mean compressive strength (Table 4), showing a serrated

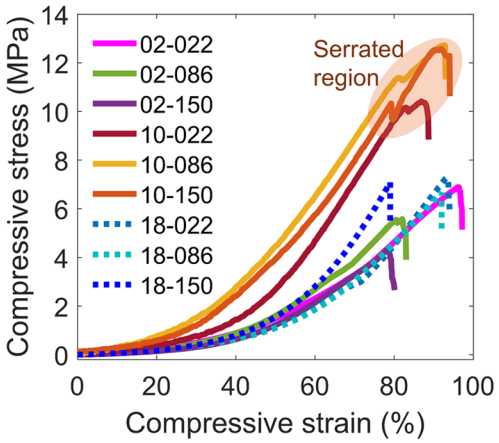


**FIGURE 7** | Representative stress–strain curves for the nine FC-CCD combinations under transverse compression. [Color figure can be viewed at wileyonlinelibrary.com]

**TABLE 4** | Compressive strength and strain at break for all FC-CCD combinations.

| Sample | Compressive strength at break (MPa) ($n = 4$) | Compressive strain at break (%) ($n = 4$) |
|---|---|---|
| 02-022 | $6.8 \pm 0.4^{ab}$ | $92 \pm 7^{a}$ |
| 02-086 | $5.5 \pm 0.5^{bc}$ | $83 \pm 2^{ab}$ |
| 02-150 | $4.5 \pm 0.4^{c}$ | $78 \pm 8^{b}$ |
| 10-022 | $10.6 \pm 1.2^{d}$ | $91 \pm 5^{ab}$ |
| 10-086 | $12.4 \pm 1.1^{e}$ | $92 \pm 3^{ab}$ |
| 10-150 | $12.4 \pm 0.6^{e}$ | $94 \pm 7^{a}$ |
| 18-022 | $6.9 \pm 0.3^{ab}$ | $91 \pm 2^{ab}$ |
| 18-086 | $6.6 \pm 0.9^{ab}$ | $93 \pm 6^{a}$ |
| 18-150 | $7.4 \pm 0.5^{a}$ | $84 \pm 11^{ab}$ |

*Note:* Means within a column sharing the same superscript letter are not significantly different ($p \leq 0.05$), and $n$ denotes the number of replicates per combination.

pattern observed near the end of the test, at approximately 10 MPa and 95% strain (Figure 7, orange ellipsis). This serration is attributed to the formation of localized fractures observed at the center of the indenter's contact length that caused temporary drops in the measured stress. However, because the material is still capable of deforming and a less defective network can redistribute stress stopping crack propagation, the stress then increases again until the next localized failure event occurs. It is interesting to note that while the compressive strength varied significantly among the formulations (4.5–12.4 MPa, Table 4), the strain at break remained consistently high overall (> 78%). The stronger samples (10:1 mix ratio) possessed a higher crosslink density (Table 3), requiring significantly higher stress to deform. However, since the failure mechanism in transverse compression is governed by geometric confinement and the ultimate shear limit of the PDMS chains, all samples were able to undergo extensive deformation before the onset of fracture, regardless of their stiffness. Despite exhibiting the lowest strength and strain at break, the 02-150 waveguides

still operated considerably beyond their linear (100 kPa) and extended linear ranges (Table S1). This suggests a safe operational margin, even when the applied compression significantly exceeds the sensing range. It is also noteworthy that, even after fracture and substantial damage along the optical path, all waveguides retained optical signal transmission. The transmitted light intensity ranged from 17% to 44% of the original value, depending on the extent of damage. This residual functionality enabled continued use by adjusting the spectrometer's integration time and applying pressure to an undamaged section of the waveguide.

To assess their behavior under repeated mechanical stress, one optical waveguide for each mix ratio cured at 150°C, i.e., 02-150, 10-150, and 18-150, was subjected to cyclic compression (Figure 8). The test protocol comprised 15 cycles across three peak stress levels: five cycles at 100 kPa (the level used

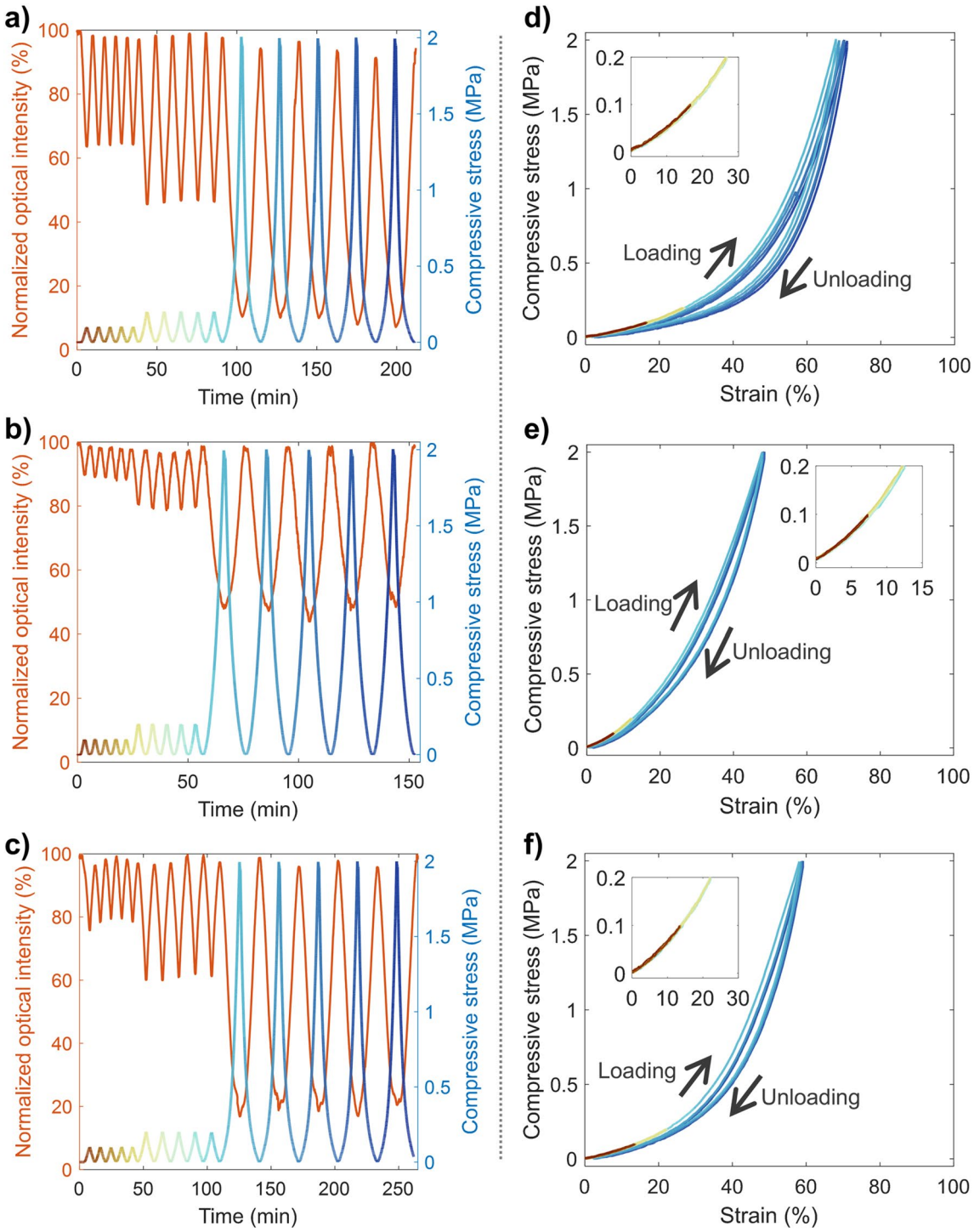


**FIGURE 8** | Cyclic compression response of waveguides 02-150, 10-150, and 18-150. (a–c) Normalized transmitted optical intensity and compressive stress versus time. (d–f) Corresponding stress–strain curves. Insets highlight the initial 5 cycles at 100 kPa followed by 5 cycles at 200 kPa. The color gradient indicates the progression of compression cycles, transitioning from red (first cycle) to dark blue (final cycle). [Color figure can be viewed at wileyonlinelibrary.com]

for sensitivity and secant modulus calculations), five cycles at 200 kPa (twice the initial limit), and five cycles at 2 MPa (approaching the optomechanical response plateau shown in Figure 2a). A 45-s holding period was implemented at the end of each loading step, and a similar recovery period was applied after each unloading step. Compression sensitivity for both loading and unloading segments was estimated using the slope of the best linear fit. Additionally, the lower and upper limits of normalized optical intensity reached during the holding and recovery periods, respectively, were assessed to verify the repeatability and consistency of the waveguides' response. For the final five cycles at 2 MPa, the linear fit was restricted to the 200 kPa range due to the non-linear optomechanical response observed at higher stresses (Figure 2a) while still allowing for a reasonable linear fit. The average sensitivity during loading and unloading, along with the lower and upper limits of normalized transmitted optical intensity, were averaged across five cycles within each compression range and are presented in Table 5.

All optical waveguides exhibited consistent sensitivity during loading and unloading up to 200 kPa, with drifts in the lower and upper limits of normalized optical intensity not exceeding 2% (Table 5, Figure 8). This indicates a repeatable optical signal response. A minor decrease (1.5%–4.0%) in the upper limit was observed after the first loading-unloading cycle for all waveguides (Figure 8a–c). This initial change is likely a combination of test setup factors, such as sample seating and adjustment, particularly during the initial phase of testing, and the material's own response, such as stress relaxation [46].

The 02-150 waveguide showed a decrease in sensitivity above 100 kPa due to a lower linearity (Table 5). It also presented an additional decrease in the upper limit of approximately 4% during the recovery period of the last five cycles within the 0–2 MPa compression range. This behavior is attributed to more pronounced stress softening compared to the other tested waveguides, as evidenced by a rightward shift in its stress–strain curve with each new cycle in the 0–2 MPa range (Figure 8d). In contrast, the other two waveguides exhibited some stress softening during the initial 0–2 MPa cycle (light blue curves in Figure 8e,f), with negligible softening afterwards. All waveguides displayed hysteresis, with the mean sensitivity during unloading from 2 MPa being consistently higher than that observed during loading (Table 5). Stress softening in PDMS is attributed to mechanisms such as chain entanglement, scission, slippage, and detachment from the filler [57, 75–77]. Meanwhile, hysteresis is ascribed to internal friction, chain relaxation and changes in free volume [57, 75]. Given that a more defective network possesses a less robust structure and higher chain mobility, it is inherently more susceptible to hysteresis and stress softening, as shown by the 02-150 waveguide in Figure 8d [57]. Nevertheless, the 02-150 waveguides demonstrated a comparable performance to the other tested waveguides up to 200 kPa, which should be considered as the operating limit range for this particular recipe.

Furthermore, while this study focuses on room temperature characterization, literature data suggests that these results remain valid across a broader temperature range. Mechanically, Sylgard 184 (1:1 mix ratio) optical waveguides exhibited a constant storage modulus between −30°C and 90°C at 3% tensile strain, indicating that the material maintains its structural stiffness across this range [23]. Optically, waveguides with a 20:1 mix ratio showed stable normalized optical transmission under 20 kPa loading, with a negligible shift from 85.9% ± 0.9% at 21°C to 85.4% ± 2% at 38°C [4]. This thermal stability is further corroborated by Sharma et al., who reported a stable optical signal in the 30°C–45°C range [3]. Moreover, unloaded 10:1 optical waveguides demonstrated a low linear optical loss of 0.0022 (dB/cm)/°C across the 24°C–70°C range, corresponding to an optical transmission drop of 0.05%/cm per degree Celsius [78]. This temperature effect can be easily compensated for by the normalized optical transmission approach employed in our study.

## 4 | Conclusion

PDMS optical waveguides were assessed using the FC-CCD, a response surface methodology, enabling a comprehensive understanding of how mix ratio and cure conditions influence key mechanical and optical properties. This approach revealed significant curvature in the response surfaces for sensitivity to transverse compression, secant modulus, and RI, while propagation loss exhibited a weak linear trend. Additionally, the

**TABLE 5** | Cyclic compression response: average sensitivity, lower and upper limits of normalized optical intensity at each compression range.

| Sample | Compression range (kPa) | *S* (−%/kPa) loading | *S* (−%/kPa) unloading | Lower limit (%) | Upper limit (%) |
|---|---|---|---|---|---|
| 02-150 | 0–100 | 0.35 ± 0.01 | 0.36 ± 0.01 | 64.0 ± 0.3 | 97.9 ± 0.5 |
| | 0–200 | 0.27 ± 0.005 | 0.27 ± 0.004 | 46.2 ± 0.5 | 98.5 ± 0.5 |
| | 0–2000 | 0.24 ± 0.01 | 0.34 ± 0.02 | 9.2 ± 1.5 | 93.9 ± 1.9 |
| 10-150 | 0–100 | 0.09 ± 0.01 | 0.09 ± 0.01 | 89.0 ± 0.6 | 97.9 ± 0.4 |
| | 0–200 | 0.09 ± 0.003 | 0.09 ± 0.004 | 79.6 ± 0.6 | 97.0 ± 0.8 |
| | 0–2000 | 0.08 ± 0.01 | 0.11 ± 0.005 | 47.4 ± 2.0 | 98.4 ± 0.6 |
| 18-150 | 0–100 | 0.20 ± 0.01 | 0.20 ± 0.01 | 78.4 ± 1.6 | 97.5 ± 1.0 |
| | 0–200 | 0.19 ± 0.01 | 0.19 ± 0.01 | 60.8 ± 0.9 | 97.9 ± 1.3 |
| | 0–2000 | 0.20 ± 0.01 | 0.23 ± 0.01 | 18.5 ± 1.5 | 97.4 ± 1.6 |

regression equations derived from this approach provide a basis for the targeted optimization of PDMS waveguide performance.

For sensitivity and secant modulus, the mix ratio was identified as the key controlling parameter, as it directly influences the PDMS network structure, followed by a statistically significant interaction between mix ratio and cure temperature. Notably, although changes in cure temperature have a smaller impact on these two properties, cure temperature presents a statistically significant effect when varied concurrently with the mix ratio within the tested ranges. Moreover, a reasonable inverse linear correlation was demonstrated between sensitivity to transverse compression and secant modulus. Considering the obtained response surface and the testing methodology, further optimization of sensitivity in PDMS optical waveguides should focus primarily on the regions surrounding the 2:1 and 10:1 mix ratios. This suggests that a curing agent-rich environment is advantageous, contrasting with the typical excess of prepolymer base often employed in other studies, particularly when combined with higher cure temperatures. Regarding the evaluated optical properties, the RI was primarily driven by cure temperature, which is attributed to changes in material density. In contrast, propagation loss showed a minor but significant dependence on mix ratio likely caused by the excess vinyl groups in the 18:1 mixture, resulting from the excess of prepolymer base.

Contrary to the expectation that room-temperature cured samples would be softer, our results indicated that the mechanical behavior of PDMS samples was less dependent on cure temperature within each tested mix ratio, likely because tests were conducted after the crosslinked networks had reached a point of relative equilibrium and most of the crosslinking reactions had occurred. However, under conditions with an excess of curing agent (2:1 mix ratio), higher cure temperatures resulted in softer optical waveguides. This is attributed to the formation of a more defective network, as corroborated by sol fraction, crosslink density, and ATR-FTIR analyses. Despite this, waveguides prepared at a 2:1 mix ratio and cured at 150°C exhibited the highest compression sensitivity with good repeatability during cyclic compression. Their ultimate mechanical properties significantly exceeded the sensor's operational linear range (primarily set at 100 kPa), offering a robust and highly sensitive option for optical pressure sensing. For applications requiring higher optical pressure ranges, waveguides with lower sensitivity but greater robustness against hysteresis and stress softening could be considered.

### Author Contributions

**Camila A. Zimmermann:** conceptualization (lead), data curation (lead), formal analysis (lead), investigation (lead), methodology (lead), software (lead), validation (lead), writing – original draft (lead), writing – review and editing (lead). **Bora Ung:** conceptualization (supporting), formal analysis (supporting), funding acquisition (lead), supervision (lead), writing – review and editing (supporting).

### Acknowledgments

C.A.Z. would like to acknowledge the use of the perceptually uniform scientific colormaps by Crameri, F. (2019). Scientific Color Maps. Zenodo. Retrieved from https://zenodo.org/record/1243862. C.A.Z. would like to thank STEPPE, LACIME, and LEM personnel from ÉTS for their assistance and support during the development of this work, in particular, Marielle Jacques, Mathieu Gratuze, and Serge Plamondon.

### Funding

This research was funded by Fonds de Recherche du Québec-Nature et Technologies (grant number 304946, DOI: 10.69777/304946), and ÉTS Research Chair in Engineering Marcelle-Gauvreau.

### Conflicts of Interest

The authors declare no conflicts of interest.

### Data Availability Statement

The data that support the findings of this study are available from the corresponding authors upon reasonable request.

### References

1. C. A. Zimmermann, K. N. Amouzou, and B. Ung, "Recent Advances in PDMS Optical Waveguides: Properties, Fabrication, and Applications," *Advanced Optical Materials* 13, no. 1 (2025): 2401975.

2. A. Leal-Junior, J. Guo, R. Min, A. J. Fernandes, A. Frizera, and C. Marques, "Photonic Smart Bandage for Wound Healing Assessment," *Photonics Research* 9, no. 3 (2021): 272.

3. K. Sharma, E. Morlec, S. Valet, et al., "Polydimethylsiloxane Based Soft Polymer Optical Fibers: From the Processing-Property Relationship to Pressure Sensing Applications," *Materials & Design* 232 (2023): 112115.

4. K. N. Amouzou, A. A. Romero, D. Sengupta, et al., "Development of High Refractive Index Polydimethylsiloxane Waveguides Doped With Benzophenone via Solvent-Free Fabrication for Biomedical Pressure Sensing," *Photonics* 9, no. 8 (2022): 557.

5. M. Choi, S. Lee, S. W. Kim, et al., "Battery-Free, Wireless Multi-Sensing Platform for Comprehensive Management of Pressure Injury and Hygiene," *Advanced Functional Materials* 35, no. 39 (2025): e06774.

6. R. Koeppe, P. Bartu, S. Bauer, and N. S. Sariciftci, "Light- and Touch-Point Localization Using Flexible Large Area Organic Photodiodes and Elastomer Waveguides," *Advanced Materials* 21, no. 34 (2009): 3510–3514.

7. W. Peng, Q. Liao, and H. Song, "A Nanograting-Based Flexible and Stretchable Waveguide for Tactile Sensing," *Nanoscale Research Letters* 16, no. 1 (2021): 23.

8. A. Levi, M. Piovanelli, S. Furlan, B. Mazzolai, and L. Beccai, "Soft, Transparent, Electronic Skin for Distributed and Multiple Pressure Sensing," *Sensors* 13, no. 5 (2013): 6578–6604.

9. L. Fliegans, J. Troughton, V. Divay, S. Blayac, and M. Ramuz, "Design, Fabrication and Characterisation of Multi-Parameter Optical Sensors Dedicated to E-Skin Applications," *Sensors* 23, no. 1 (2022): 114.

10. M. Ramuz, B. C. K. Tee, J. B. H. Tok, and Z. Bao, "Transparent, Optical, Pressure-Sensitive Artificial Skin for Large-Area Stretchable Electronics," *Advanced Materials* 24, no. 24 (2012): 3223–3227.

11. C.-H. Mak, Y. Li, K. Wang, et al., "Intelligent Shape Decoding of a Soft Optical Waveguide Sensor," *Advanced Intelligent Systems* 6, no. 2 (2024): 2300082.

12. J. Guo, M. Niu, and C. Yang, "Highly Flexible and Stretchable Optical Strain Sensing for Human Motion Detection," *Optica* 4, no. 10 (2017): 1285–1288.

13. L. Bahin, M. Tourlonias, M.-A. Bueno, K. Sharma, and R. M. Rossi, "Smart Textiles With Polymer Optical Fibre Implementation for In-Situ Measurements of Compression and Bending," *Sensors and Actuators, A: Physical* 350 (2023): 114117.

14. C. Guignier, B. Camillieri, M. Schmid, R. M. Rossi, and M.-A. Bueno, "E-Knitted Textile With Polymer Optical Fibers for Friction and Pressure Monitoring in Socks," *Sensors (Basel)* 19, no. 13 (2019): 3011.

15. B. M. Quandt, R. Hufenus, B. Weisse, et al., "Optimization of Novel Melt-Extruded Polymer Optical Fibers Designed for Pressure Sensor Applications," *European Polymer Journal* 88 (2017): 44–55.

16. M. Rothmaier, M. P. Luong, and F. Clemens, "Textile Pressure Sensor Made of Flexible Plastic Optical Fibers," *Sensors* 8, no. 7 (2008): 4318–4329.

17. J. Gan, A. Yang, Q. Guo, and Z. Yang, "Flexible Optical Fiber Sensing: Materials, Methodologies, and Applications," *Advanced Devices & Instrumentation* 5 (2024): 0046.

18. J. Zubia, J. Arrue, and A. Mendioroz, "Theoretical Analysis of the Torsion-Induced Optical Effect in a Plastic Optical Fiber," *Optical Fiber Technology* 3, no. 2 (1997): 162–167.

19. Y. Wan, Y. Wang, and C. F. Guo, "Recent Progresses on Flexible Tactile Sensors," *Materials Today Physics* 1 (2017): 61–73.

20. Z. Huang, Y. Xu, Y. Cheng, et al., "Recent Advances in Skin-Like Wearable Sensors: Sensor Design, Health Monitoring, and Intelligent Auxiliary," *Sensors & Diagnostics* 1 (2022): 686–708.

21. S. Poeggel, D. Tosi, D. Duraibabu, G. Leen, D. McGrath, and E. Lewis, "Optical Fibre Pressure Sensors in Medical Applications," *Sensors* 15, no. 7 (2015): 17115–17148.

22. J. E. Mark, ed., *Polymer Data Handbook* (Oxford University Press, 1999).

23. K. Sharma, W. Wang, S. Valet, et al., "Microfluidic Wet Spinning of Soft Polydimethylsiloxane Polymer Optical Fibers," *Materials & Design* 248 (2024): 113466.

24. M. A. Andersen and J. Schouenborg, "Polydimethylsiloxane as a More Biocompatible Alternative to Glass in Optogenetics," *Scientific Reports* 13, no. 1 (2023): 16090.

25. Y. Cao, S. Pan, M. Yan, et al., "Flexible and Stretchable Polymer Optical Fibers for Chronic Brain and Vagus Nerve Optogenetic Stimulations in Free-Behaving Animals," *BMC Biology* 19, no. 1 (2021): 1–13.

26. F. Saleheen, J. Goldstein, R. Rajan, D. Caroline, S. Pascarella, and C. Won, "Smartphone-Based Compression-Induced Scope With Temperature Sensor for Inflammatory Breast Cancer Screening," in *2018 40th Annu. Int. Conf. IEEE Eng. Med. Biol. Soc. EMBC* (IEEE, 2018), 4969–4972.

27. D. Rus and M. T. Tolley, "Design, Fabrication and Control of Soft Robots," *Nature* 521, no. 7553 (2015): 467–475.

28. S. C. B. Mannsfeld, B. C.-K. Tee, R. M. Stoltenberg, et al., "Highly Sensitive Flexible Pressure Sensors With Microstructured Rubber Dielectric Layers," *Nature Materials* 9, no. 10 (2010): 859–864.

29. K. Lim, J. Lee, S. Kim, et al., "Interference Haptic Stimulation and Consistent Quantitative Tactility in Transparent Electrotactile Screen With Pressure-Sensitive Transistors," *Nature Communications* 15, no. 1 (2024): 7147.

30. A. F. T. Mak, M. Zhang, and E. W. C. Tam, "Biomechanics of Pressure Ulcer in Body Tissues Interacting With External Forces During Locomotion," *Annual Review of Biomedical Engineering* 12, no. 1 (2010): 29–53.

31. D. J. Lott, D. Zou, and M. J. Mueller, "Pressure Gradient and Subsurface Shear Stress on the Neuropathic Forefoot," *Clinical Biomechanics* 23, no. 3 (2008): 342–348.

32. M. R. Halawa, Y. M. Eid, R. A. El-Hilaly, M. M. Abdelsalam, and A. H. Amer, "Relationship of Planter Pressure and Glycemic Control in Type 2 Diabetic Patients With and Without Neuropathy," *Diabetes and Metabolic Syndrome: Clinical Research and Reviews* 12, no. 2 (2018): 99–104.

33. Y. Zhang, X. Li, J. Kim, et al., "Thermally Drawn Stretchable Electrical and Optical Fiber Sensors for Multimodal Extreme Deformation Sensing," *Advanced Optical Materials* 9, no. 6 (2021): 1–9.

34. A. Leber, B. Cholst, J. Sandt, N. Vogel, and M. Kolle, "Stretchable Thermoplastic Elastomer Optical Fibers for Sensing of Extreme Deformations," *Advanced Functional Materials* 29, no. 5 (2019): 1–8.

35. S. Shabahang, F. Clouser, F. Shabahang, and S.-H. Yun, "Single-Mode, 700%-Stretchable, Elastic Optical Fibers Made of Thermoplastic Elastomers," *Advanced Optical Materials* 9, no. 12 (2021): 2100270.

36. P. Mazurek, S. Vudayagiri, and A. L. Skov, "How to Tailor Flexible Silicone Elastomers With Mechanical Integrity: A Tutorial Review," *Chemical Society Reviews* 48, no. 6 (2019): 1448–1464.

37. A. S. Cruz-Félix, A. Santiago-Alvarado, J. Márquez-García, and J. González-García, "PDMS Samples Characterization With Variations of Synthesis Parameters for Tunable Optics Applications," *Heliyon* 5, no. 12 (2019): e03064.

38. A. Santiago-Alvarado, A. S. Cruz-Félix, J. González-García, O. Sánchez-López, A. J. Mendoza-Jasso, and I. Hernández-Castillo, "Polynomial Fitting Techniques Applied to Opto-Mechanical Properties of PDMS Sylgard 184 for Given Curing Parameters," *Materials Research Express* 7, no. 4 (2020): 045301.

39. H. S. Cho, H.-Y. Moon, H. S. Lee, Y. T. Kim, and S. C. Jeoung, "Formulation Prediction for Young's Modulus of Poly(Dimethylsiloxane) by Spectroscopic Methods," *Bulletin of the Korean Chemical Society* 42, no. 9 (2021): 1225–1231.

40. V. Prajzler, P. Nekvindova, J. Spirkova, and M. Novotny, "The Evaluation of the Refractive Indices of Bulk and Thick Polydimethylsiloxane and Polydimethyl-Diphenylsiloxane Elastomers by the Prism Coupling Technique," *Journal of Materials Science: Materials in Electronics* 28, no. 11 (2017): 7951–7961.

41. Z. Cai, W. Qiu, G. Shao, and W. Wang, "A New Fabrication Method for All-PDMS Waveguides," *Sensors and Actuators A: Physical* 204 (2013): 44–47.

42. H. Varner and T. Cohen, "Explaining the Spread in Measurement of PDMS Elastic Properties: Influence of Test Method and Curing Protocol," *Soft Matter* 20, no. 46 (2024): 9174–9183.

43. D. C. Montgomery, *Design and Analysis of Experiments* (John Wiley & Sons, Inc, 2013).

44. A. Dean, D. Voss, and D. Draguljić, *Design and Analysis of Experiments* (Springer International Publishing, 2017).

45. T. Bardelli, C. Marano, and F. Briatico Vangosa, "Polydimethylsiloxane Crosslinking Kinetics: A Systematic Study on Sylgard184 Comparing Rheological and Thermal Approaches," *Journal of Applied Polymer Science* 138, no. 39 (2021): 51013.

46. S. Zhang, C. Ge, and R. Liu, "Mechanical Characterization of the Stress-Strain Behavior of the Polydimethylsiloxane (PDMS) Substate of Wearable Strain Sensors Under Uniaxial Loading Conditions," *Sensors and Actuators, A: Physical* 341 (2022): 113580.

47. R. Seghir and S. Arscott, "Extended PDMS Stiffness Range for Flexible Systems," *Sensors and Actuators A: Physical* 230 (2015): 33–39.

48. A. Mata, A. J. Fleischman, and S. Roy, "Characterization of Polydimethylsiloxane (PDMS) Properties for Biomedical Micro/Nanosystems," *Biomedical Microdevices* 7, no. 4 (2005): 281–293.

49. Z. Wang, A. A. Volinsky, and N. D. Gallant, "Crosslinking Effect on Polydimethylsiloxane Elastic Modulus Measured by Custom-Built Compression Instrument," *Journal of Applied Polymer Science* 131, no. 22 (2014): 1–4.

50. The Dow Chemical Company, *Technical Data Sheet: SYLGARD 184 Silicone Elastomer* (Dow Chemical Company, 2017).

51. J. Guo, B. Zhou, C. Yang, Q. Dai, and L. Kong, "Stretchable and Temperature-Sensitive Polymer Optical Fibers for Wearable Health Monitoring," *Advanced Functional Materials* 29, no. 33 (2019): 1–8.

52. H. Hocheng, C. M. Chen, Y. C. Chou, and C. H. Lin, "Study of Novel Electrical Routing and Integrated Packaging on Bio-Compatible Flexible Substrates," *Microsystem Technologies* 16, no. 3 (2010): 423–430.

53. M. Odeh, B. Voort, A. Anjum, B. Paredes, C. Dimas, and M. S. Dahlem, "Gradient-Index Optofluidic Waveguide in Polydimethylsiloxane," *Applied Optics* 56, no. 4 (2017): 1202–1206.

54. ASTM, D3767-03— Standard Practice for Rubber—Measurement of Dimensions. 2020: 1–8.

55. L. K. Hillbrick, J. Kaiser, M. G. Huson, et al., "Determination of the Transverse Modulus of Cylindrical Samples by Compression Between Two Parallel Flat Plates," *SN Applied Sciences* 1, no. 7 (2019): 1–11.

56. J. N. Lee, C. Park, and G. M. Whitesides, "Solvent Compatibility of Poly(Dimethylsiloxane)-Based Microfluidic Devices," *Analytical Chemistry* 75, no. 23 (2003): 6544–6554.

57. S. Krpovic, K. Dam-Johansen, and A. L. Skov, "Importance of Mullins Effect in Commercial Silicone Elastomer Formulations for Soft Robotics," *Journal of Applied Polymer Science* 138, no. 19 (2021): 50380.

58. T. Bardelli, C. Marano, and F. Briatico Vangosa, "Influence of Curing Thermal History on Cross-Linking Degree of a Polydimethylsiloxane: Swelling and Mechanical Analyses," *Express Polymer Letters* 16, no. 9 (2022): 924–932.

59. C. Robert, A. Crespy, S. Bastide, et al., "Rheological Properties of Silicon Polymer Networks: The Influence of the Crosslink Density," *Journal of Applied Polymer Science* 87, no. 7 (2003): 1152–1160.

60. S. O. Kasap, "Chapter 9: Optical Properties of Materials," in *Principles of Electronic Materials and Devices* (McGraw-Hill Education, 2018), 859–940.

61. W. S. Lee, K. S. Yeo, A. Andriyana, Y. G. Shee, and F. R. Mahamd Adikan, "Effect of Cyclic Compression and Curing Agent Concentration on the Stabilization of Mechanical Properties of PDMS Elastomer," *Materials & Design* 96 (2016): 470–475.

62. ASTM D638-14—Standard Test Method for Tensile Properties of Plastics. 2014: 1–17.

63. F. Gaudière, I. Masson, S. Morin-Grognet, et al., "Mechano-Chemical Control of Cell Behaviour by Elastomer Templates Coated With Biomimetic Layer-By-Layer Nanofilms," *Soft Matter* 8, no. 32 (2012): 8327.

64. A. Sharfeddin, A. A. Volinsky, G. Mohan, and N. D. Gallant, "Comparison of the Macroscale and Microscale Tests for Measuring Elastic Properties of Polydimethylsiloxane," *Journal of Applied Polymer Science* 132, no. 42 (2015): app.42680.

65. J. D. Glover, C. E. McLaughlin, M. K. McFarland, and J. T. Pham, "Extracting Uncrosslinked Material From Low Modulus Sylgard 184 and the Effect on Mechanical Properties," *Journal of Polymer Science* 58, no. 2 (2020): 343–351.

66. R. Hopf, L. Bernardi, J. Menze, M. Zündel, E. Mazza, and A. E. Ehret, "Experimental and Theoretical Analyses of the Age-Dependent Large-Strain Behavior of Sylgard 184 (10:1) Silicone Elastomer," *Journal of the Mechanical Behavior of Biomedical Materials* 60 (2016): 425–437.

67. V. Placet and P. Delobelle, "Mechanical Properties of Bulk Polydimethylsiloxane for Microfluidics Over a Large Range of Frequencies and Aging Times," *Journal of Micromechanics and Microengineering* 25, no. 3 (2015): 035009.

68. D. A. Chang-Yen, R. K. Eich, and B. K. Gale, "A Monolithic PDMS Waveguide System Fabricated Using Soft-Lithography Techniques," *Journal of Lightwave Technology* 23, no. 6 (2005): 2088–2093.

69. J. Feng, Y. Zheng, Q. Jiang, M. K. Włodarczyk-Biegun, S. Pearson, and A. del Campo, "Elastomeric Optical Waveguides by Extrusion Printing," *Advanced Materials Technologies* 7, no. 10 (2022): 2101539.

70. L. Y. Tyng, M. R. Ramli, M. B. H. Othman, R. Ramli, Z. A. M. Ishak, and Z. Ahmad, "Effect of Crosslink Density on the Refractive Index of a Polysiloxane Network Based on 2,4,6,8-Tetramethyl-2,4,6, 8-Tetravin ylcyclotetrasiloxane," *Polymer International* 62, no. 3 (2013): 382–389.

71. M. A. Brook, H.-U. Saier, J. Schnabel, K. Town, and M. Maloney, "Pretreatment of Liquid Silicone Rubbers to Remove Volatile Siloxanes," *Industrial & Engineering Chemistry Research* 46, no. 25 (2007): 8796–8805.

72. A. Leal-Junior, V. Campos, A. Frizera, and C. Marques, "Low-Cost and High-Resolution Pressure Sensors Using Highly Stretchable Polymer Optical Fibers," *Materials Letters* 271 (2020): 127810.

73. W. Chassé, M. Lang, J.-U. Sommer, and K. Saalwächter, "Cross-Link Density Estimation of PDMS Networks With Precise Consideration of Networks Defects," *Macromolecules* 45, no. 2 (2012): 899–912.

74. D. Cai, A. Neyer, R. Kuckuk, and H. M. Heise, "Raman, Mid-Infrared, Near-Infrared and Ultraviolet–Visible Spectroscopy of PDMS Silicone Rubber for Characterization of Polymer Optical Waveguide Materials," *Journal of Molecular Structure* 976, no. 1–3 (2010): 274–281.

75. D. E. Hanson, M. Hawley, R. Houlton, et al., "Stress Softening Experiments in Silica-Filled Polydimethylsiloxane Provide Insight Into a Mechanism for the Mullins Effect," *Polymer* 46, no. 24 (2005): 10989–10995.

76. J. M. Clough, C. Creton, S. L. Craig, and R. P. Sijbesma, "Covalent Bond Scission in the Mullins Effect of a Filled Elastomer: Real-Time Visualization With Mechanoluminescence," *Advanced Functional Materials* 26, no. 48 (2016): 9063–9074.

77. F. Clément, L. Bokobza, and L. Monnerie, "On the Mullins Effect in Silica-Filled Polydimethylsiloxane Networks," *Rubber Chemistry and Technology* 74, no. 5 (2001): 847–870.

78. C. A. Zimmermann, K. N. Amouzou, D. Sengupta, A. Kumar, N. R. Demarquette, and B. Ung, "Novel Elastomeric Spiropyran-Doped Poly(Dimethylsiloxane) Optical Waveguide for UV Sensing," *Frontiers of Optoelectronics* 17, no. 1 (2024): 21.

**Supporting Information**

Additional supporting information can be found online in the Supporting Information section. **Data S1:** Supporting Information.